

Inverse-Compton emission from the lobes of 3C 353

J.L. Goodger,^{1*} M.J. Hardcastle,¹ J.H. Croston,¹ N.E. Kassim² and R.A. Perley³

¹University of Hertfordshire, College Lane, Hatfield, Hertfordshire AL10 9AB, UK

²US Naval Research Lab 4555 Overlook Ave., SW Washington, DC 20375, USA

³National Radio Astronomy Observatory, P.O. Box O, Socorro, NM 87801, USA

ABSTRACT

X-ray emission due to inverse-Compton scattering of microwave background photons by electrons in the lobes of powerful radio galaxies has now been seen in a large number of objects. Combining an inverse-Compton model for the lobe X-ray emission with information obtained from radio synchrotron emission provides a method of constraining the electron population and magnetic field energy density, which cannot be accomplished using the radio data alone. Using six frequencies of new and archival radio data and new *XMM-Newton* observations of the Fanaroff & Riley class II radio galaxy 3C 353, we show that inverse-Compton emission is detected in the radio lobes of this source at a level consistent with what is seen in other objects. We argue that variations in the X-ray/radio ratio in the brighter eastern lobe require positionally varying magnetic field strength. We also examine the X-ray nucleus and the cluster, Zw 1819.1-0108, spatially and spectrally.

Key words:

galaxies: active – X-rays: galaxies – galaxies: individual: 3C 353 – galaxies: jets – radiation mechanisms: non-thermal: X-ray: galaxies: clusters

1 INTRODUCTION

Extended X-ray emission from the lobes of powerful, FR II (Fanaroff & Riley 1974) radio galaxies and quasars is thought to be produced by inverse-Compton scattering of the cosmic microwave background (CMB) (Feigelson et al. 1995; Tashiro et al. 1998; Tashiro et al. 2001; Isobe et al. 2002; Hardcastle et al. 2002) and of infrared photons from the core (Brunetti, Setti & Comastri 1997). Although the synchrotron self-Compton emission from the lobes can also be modelled, it is negligible compared to the inverse-Compton emission from other populations except in the very small-est lobes (Hardcastle et al. 2002). Recent studies of the integrated X-ray properties of radio lobes have been carried out for large samples (Croston et al. 2005; Kataoka & Stawarz 2005), showing that the CMB is the dominant photon population in most cases. Combining an inverse-Compton/CMB model for the lobe X-ray emission with information obtained from radio synchrotron emission provides a method of constraining the electron population and magnetic field energy density, which cannot be accomplished using radio data alone. Unlike the jets, the lobe material is not moving relativistically so there are no beaming effects to consider during this analysis (e.g. Mackay 1973). Understanding the contributions of the electron densities of the synchrotron and inverse-Compton electron populations and the magnetic field allows us to estimate directly the total energy in the radio source, and thus the amount of

energy that can be transferred to the environment, without assuming equipartition, and also allows us to investigate the distribution of internal energy within the source.

Hardcastle & Croston (2005) recently carried out a spatially resolved X-ray inverse-Compton study of the bright X-ray and radio source Pictor A. They used the variation of the X-ray/radio ratio across the lobes to investigate the variation in electron density and magnetic field strength throughout the source. They found that variations in either component alone could not explain the observed X-ray and radio properties of the lobe. Similar spatially resolved X-ray studies of other bright FR II radio galaxies are needed to follow up these results. Here we report on observations of the radio galaxy 3C 353.

3C 353 is a FR II radio galaxy associated with the cluster Zw 1718.1-0108. Although it is one of the brightest extragalactic sources in the sky at low frequencies, it is relatively poorly studied, presumably due to its low declination and low Galactic latitude. Swain (1996) observed 3C 353 at four radio frequencies with the NRAO Very Large Array (VLA) and published a study of the polarisation variation across the jets, which favoured a spine-sheath model (Swain, Bridle & Baum 1998). Their VLA observations revealed filamentary structure within the lobes making 3C 353 an excellent target for a spatially resolved study of electron distribution and magnetic fields. X-ray emission from the cluster associated with 3C 353 was first detected by Iwasawa et al. (2000) in *ASCA* and *ROSAT* images. The radio source resides in a giant elliptical galaxy on the edge of the cluster, which Iwasawa et al. found to be bright in the X-ray with a luminous point source coinciding with

* E-mail: j.l.goodger@herts.ac.uk

the radio galaxy's core. Iwasawa et al. determined global cluster temperatures and used optical observations to identify the cluster's members. They confirmed a redshift of $z = 0.0304$ for 3C 353, a redshift of $z = 0.028$ for three bright member galaxies, and used the velocity distribution to confirm 3C 353 as a member of the same system.

In this paper we use new *XMM-Newton* and radio observations to investigate the nature of the electron distribution and the magnetic fields in the lobes and hotspots of 3C 353. We also determine the cluster temperature, density and pressure profiles and examine the cluster's interaction with the lobes of 3C 353. Throughout the paper we use a cosmology in which $H_0 = 70 \text{ km s}^{-1} \text{ Mpc}^{-1}$, $\Omega_m = 0.3$, and $\Omega_\Lambda = 0.7$. The angular scale is $1 \text{ arcsec} = 0.61 \text{ kpc}$. We define the spectral index in the sense that $S_\nu \propto \nu^{-\alpha}$. The photon index $\Gamma = 1 + \alpha$.

2 DATA

We used a combination of new and archival radio data and new *XMM-Newton* X-ray data to examine the broad-spectrum electron energy distribution of 3C 353. Our radio data extends to lower frequencies than have been studied previously, whilst our X-ray data has greatly improved sensitivity and resolution compared to the ASCA data of Iwasawa et al. (2000).

2.1 Radio

We obtained VLA observations at 1.6 GHz and 4.8 GHz from the VLA archive as well as carrying out new observations at 327 MHz at the VLA and at 620 MHz at the NCRA Giant Meter-wave Radio Telescope (GMRT) in 2006. We also obtained images of 3C 353 at 74 MHz and 8.4 GHz (see below). All the radio data were reduced in AIPS. The radio observations are summarized in Table 1 and Fig. 1 shows an example of the image quality achieved.

2.1.1 4 Band; 74 MHz, 4 m

The 74-MHz observations used are those discussed by Kassim et al. (2007) and the data reduction is described in that paper.

2.1.2 P Band; 327 MHz, 91 cm

Our 327 MHz observations of 3C 353 were taken at the VLA on the 27th May 2006 using the nearby Pie Town antenna of the Very Large Baseline Array (VLBA) to increase the long baseline of our A configuration data set by a factor of two. We carefully monitored the Pie Town antenna during the calibration steps to ensure that the long baselines survived.

Initial bandpass calibration using 3C 286 resulted in smooth phase and amplitude variation across all channels. As a flux calibrator, 3C 286 is slightly resolved at this frequency. If the fractional bandwidth is great enough that the intrinsic visibility of 3C 286 varies across the pass band, a model is required (Lazio et al. 2005). At 327 MHz with the Pie Town antenna, we found that this effect is negligible so 3C 286 was used as the flux calibrator without a model, effectively treated as a point source. 3C 286 was used to calibrate the phase across all baselines. The resultant calibrated data set was flagged to remove noise then spectrally averaged using SPLAT, averaging every 4 channels to reduce the number of channels to 6, whilst producing a single source data set. The calibrated

data included baselines up to 80 k λ , twice what would have been achieved with only the A configuration.

The B-configuration data set was bandpass calibrated using 3C 286 to calibrate the channel gains, then flux using 3C 286 and phase calibrated with 1416 + 067. After flagging and phase cross-calibrating with the A configuration data set, the data sets were merged and a multi-facet deep cleaned map of 106 fields was produced. The dynamic range of the final map is 580:1 with a resolution of $6.7 \times 2.9 \text{ arcsec}$.

2.1.3 620 MHz, 48 cm

Our 620 MHz observations were taken at the GMRT on 19th July 2006. The two observing frequencies (upper and lower sidebands) were calibrated separately. Preliminary bandpass calibration was performed using 3C 286 followed by flagging and one iteration of *flagit* to remove RFI from all sources. This flagged data set was then bandpass- and flux-calibrated before being manually flagged and another iteration of *flagit* applied. The data set was spectrally averaged into a multi-source data set, cutting the number of channels from 128 to 6, whilst applying the bandpass calibration. This data set was finally flux- and phase-calibrated before 3C 353 was *split* into a single-source file. The flux and phase calibrator used was 1743-038. One iteration of phase self-calibration was performed before the data from the two observing frequencies were split into individual channels and recombined using DBCON to a single data set containing all of the averaged channels. This combined data set was phase self-calibrated twice more and the final image has resolution 7.50×4.41 and dynamic range 590 : 1.

2.1.4 L Band; 1.67 GHz, 22 cm

Observations from A-, B- and C-configurations were flux- and phase-calibrated separately using NRAO530 as the phase calibrator. Due to the allocation of the observing frequencies in the C-configuration data set, the data at the two frequencies were split and recombined using DBCON to match the frequency allocations of the A- and B-configuration data sets. Once combined, the data were phase self-calibrated and deep cleaned, with 100,000 iterations of CLEAN applied. The final image has a resolution of $1.7 \times 1.4 \text{ arcsec}$ and a dynamic range of 500 : 1.

2.1.5 C Band; 4.8 GHz, 6.3 cm

For maximum *uv* coverage, we use B-, C- and D-configuration data sets, each of which were phase- and flux-calibrated and flagged. We combine two epochs of D-configuration observations to increase the signal to noise.

The final combined data set was phase and amplitude self-calibrated, normalizing the gain. There was no significant reduction in the maximum flux when compared to phase-only self-calibration, but the image quality was improved. The final image has a resolution $2.24 \times 1.81 \text{ arcsec}$ and a dynamic range of 1180:1.

2.1.6 X Band; 8.4 GHz, 3.6 cm

The X band images of 3C 353 were kindly provided by Alan Bridle. The deep cleaned images have a dynamic range of 2500:1 and a resolution of $1.30 \times 1.30 \text{ arcsec}$. The details of the reduction are described by Swain (1996).

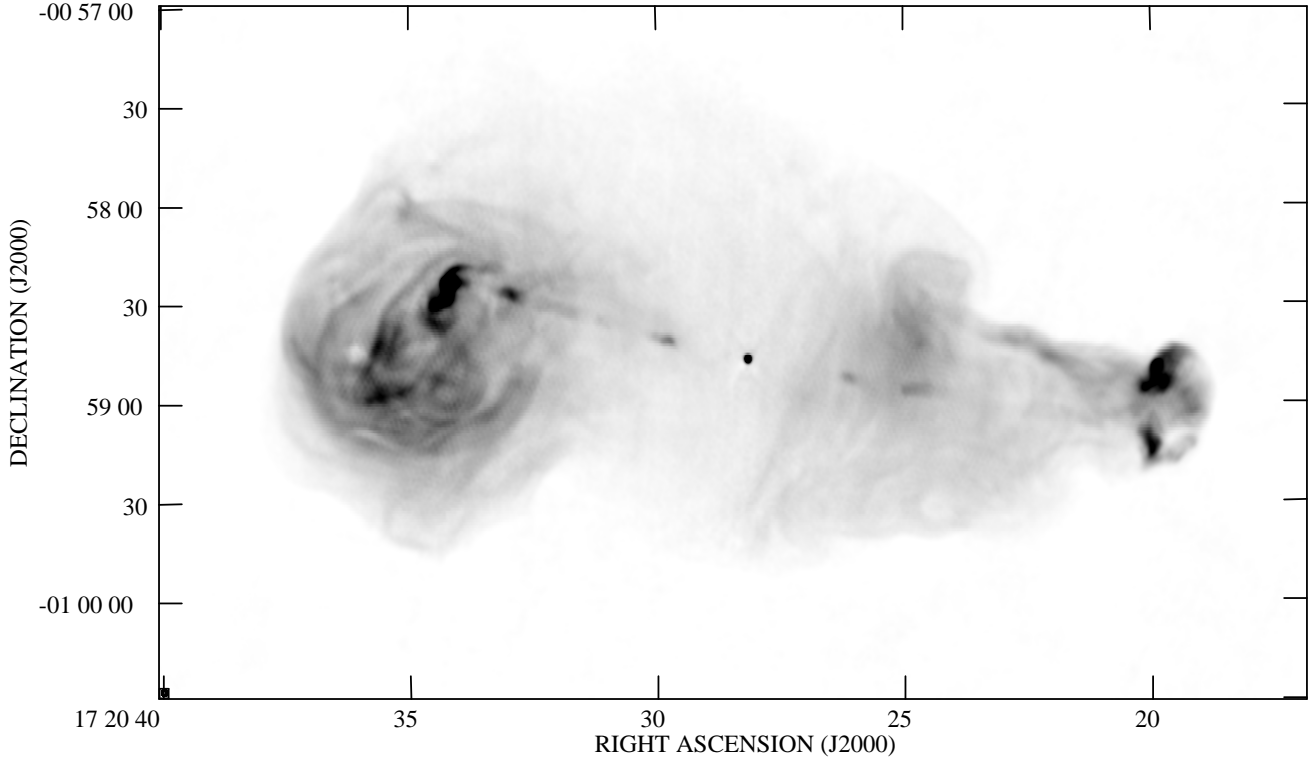


Figure 1. 1.67 GHz total intensity image of 3C 353 at 1.8 arcsec resolution

Table 1. Radio Observation Details

Band	Frequency (MHz)	Telescope:Config.	Date	Duration (s)	Bandwidth (MHz)	Phase Calibrator	Dynamic Range	Res. (arcsec)
4	73.8	VLA	07/03/1998	7740	1.3	3C405	2090:1	25.0×25.0
P	327.3	VLA:A+PT	27/05/2006	25660	3.125	3C286	580:1	6.75×2.92
		VLA:B	04/10/1998	3010	0.098	1416+067		
-	614	GMRT	19/07/2006	19847	16.0	1743-038	590:1	6.41×4.27
L	1665/1385	VLA:A	19/05/1968	20710	12.5	NRAO530	500:1	1.78×1.44
		VLA:B	14/08/1968	6640	25.0	NRAO530		
		VLA:C	16/09/1985	1441	50.0	1741-038		
C	4848/4898	VLA:B	14/08/1986	6799	50.0	NRAO530	1180:1	2.24×1.81
		VLA:C	22/08/1985	1679	50.0	1741-038		
		VLA:D	15/11/1993	532	50.0	1730-130		
		VLA:D	28/09/1984	3360	50.0	1725+044		
X	8440/8452	VLA:BCnD	13/03/1994		12.5		2500:1	1.30×1.30

2.2 X-ray

We observed 3C 353 on the 25th August 2006 and 17th February 2007 with *XMM-Newton* EPIC MOS1, MOS2 and pn cameras. The initial observation (Set 1) from 25th August 2006 yielded 39 522 s and 39 525 s for MOS1 and MOS2 respectively and 34 042 s for the pn camera, whereas the second observation on the 17th February 2007 (Set 2) was for 10 473 s and 10 487 s for MOS1 and MOS2 and 5 653 s for pn. The pn camera was in Extended Full Frame mode for both observations and the MOS cameras were in Full Frame mode.

The data sets were initially processed using SAS version 7.0.0. Standard EPIC MOS and PN pipelines and the standard filters

#XMMEA_EA and #XMMEA_EP were applied. The MOS data sets were filtered to include single, double, triple and quadruple events ($\text{PATTERN} \leq 12$) whereas the PN data set was filtered to include only single and double events ($\text{PATTERN} \leq 4$). Set 1 MOS data sets were free from flare events whilst the PN data set was filtered with a count threshold of 2 counts per second to remove a small flare event at the end of the observation. In Set 2, all cameras were affected by flaring; the MOS and PN data sets were filtered with count rate thresholds of 0.3 and 0.7 counts per second respectively. As only 1510 seconds remained of the PN data, this data set was excluded from further analysis. The net livetimes for Sets 1 and 2 were 44 039 for MOS1 and MOS2 and 26 052 for PN.

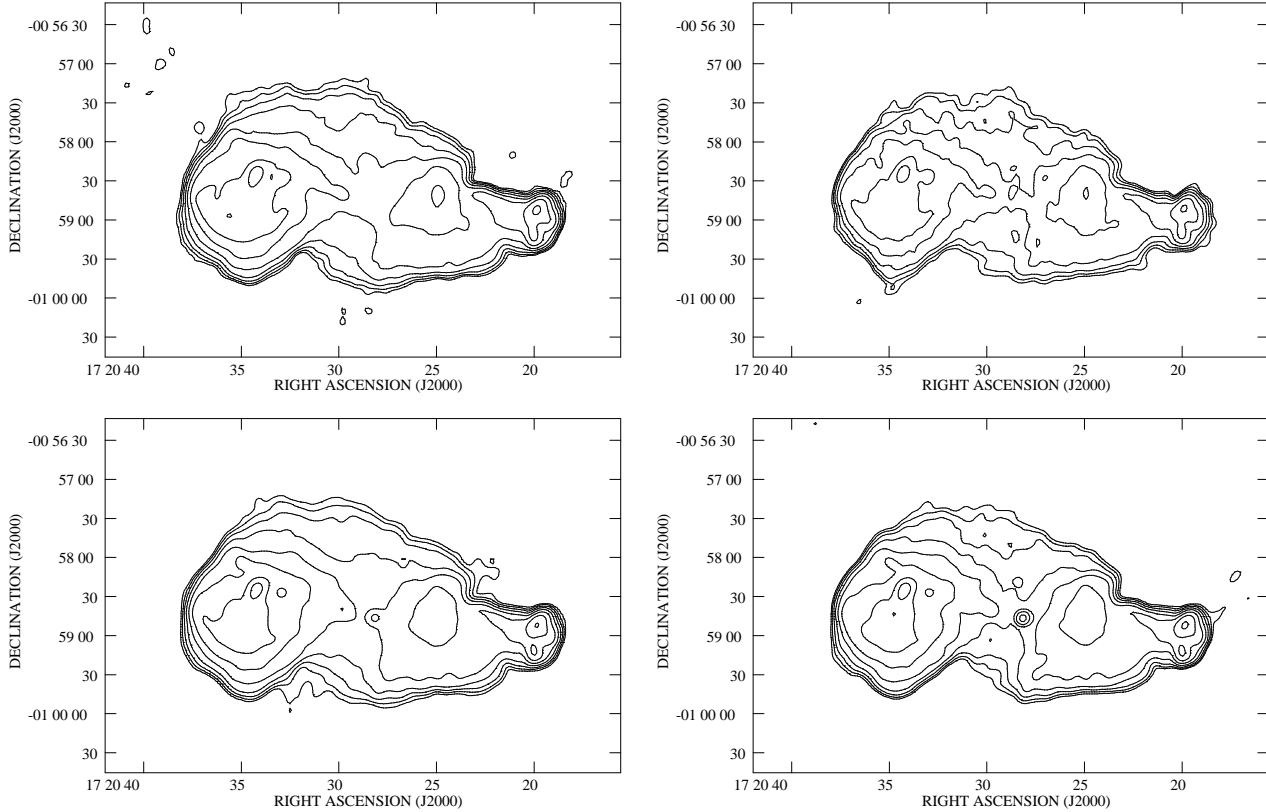


Figure 2. Radio contour images of 3C 353 at 327 MHz (top left), 620 MHz (top right), 1.67 GHz (bottom left) and 4.8 GHz (bottom right) all convolved to 7.5×7.5 arcsec resolution. The contour levels are at $5\sigma \times (1, 2, 4, \dots)$ mJy/beam where $5\sigma = 0.0106$ for 327 MHz, 0.0113 for 620 MHz, 0.0045 for 1.67 GHz and 0.0017 for 4.8 GHz.

The MOS and PN data sets were energy filtered to include energies between 0.5 and 5 keV before using the SAS command *evselect* to generate images from the filtered events files. The task *exmap* was then used to generate exposure maps without vignetting. We chose not to include vignetting correction in these images as it incorrectly weights up the particle background at the edge of the field, creating artefacts in the image. The images from the separate detectors were normalized to the Set 1 PN count rate (in order to remove the PN chip gaps) and then combined. The exposure maps were combined then divided by the total filtered live-time. The combined normalised image was finally divided by the scaled combined exposure map. The combined image was Gaussian smoothed with a kernel of 10.4 arcsec to highlight the clusters and radio lobes using the CIAO command *aconvolve*.

X-ray spectra were extracted using *especget*, a script that combines the *evselect*, *arfgen* and *rmfgen* commands in SAS, from regions defined to examine the emission from the northern and southern sub-cluster regions, and the east and west lobes. As the core and lobes are small regions near the pointing centre, so that vignetting is not important, we used local background subtraction. However, for the cluster, vignetting needs to be considered. The filtered event files were weighted using *evweight* before spectra were extracted using a double subtraction method, (e.g. Arnaud et al. 2002). Background template files for the field of view were made using files created by Read & Ponman (2003) and scaled to the same particle background level as our observations. A local background region away from the galaxy and cluster was defined using DS9. A template background spectrum was subtracted from the source spec-

trum events file to account for instrument and particle noise before a local background region was used to subtract residual background emission due to the differences in the Galactic/extragalactic background levels of the source and scaled background datasets. Due to the low signal to noise of Set 2, only Set 1 could be used in the double subtraction method applied to the cluster. The spectra were then binned to 20 counts per channel after background subtraction, ignoring the first 20 channels for the MOS cameras and the first 50 channels for the pn camera.

3 RESULTS

In this section we discuss the results of the X-ray spectral fitting and radio flux density measurements. X-ray fitting was carried out using XSPEC v 11.3 in the energy range 0.3 – 7.0 keV. Where thermal models were fitted we used a redshift of 0.03.

3.1 Absorbing column density

The column density towards 3C 353 is uncertain. Iwasawa et al. (2000) adopt a value of $1.0 \times 10^{21} \text{ cm}^{-2}$ based on the H I measurements of Dickey & Lockman (1990). However, they note that the visual extinction in the direction of 3C 353 would correspond to a column density of a factor ~ 2 higher. From the Galactic dust measurements of Schlegel et al. (1998) we estimate an A_V of 1.4 mag, which would correspond to a column density of $\sim 2.6 \times 10^{21}$

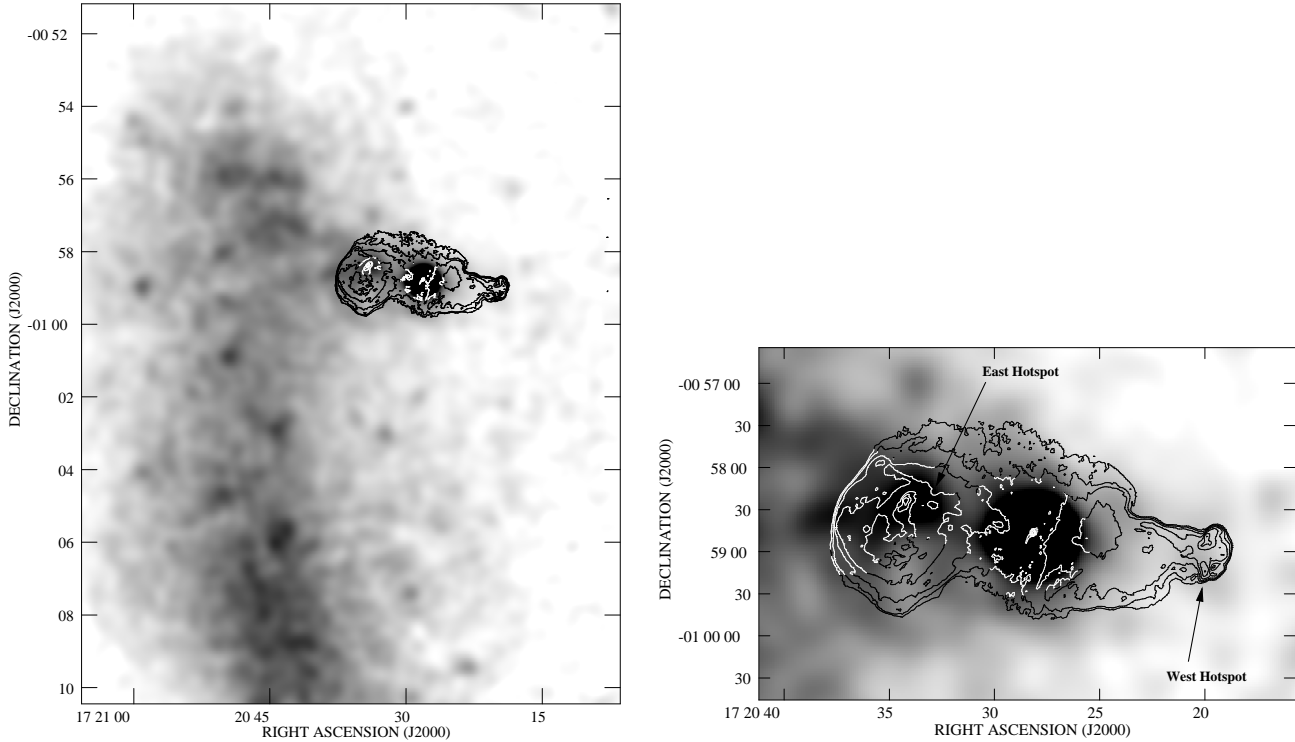


Figure 3. Radio contours of 3C 353 at 1.67 GHz with a 0.3-7.0 keV *XMM-Newton* image (MOS 1, MOS 2 + pn) of the X-ray emission from the radio lobes and the cluster Zw 1718.1-0108 (left) Gaussian smoothed with a kernel of 10.4 arcsec; the same image zoomed in to show the inverse-Compton emission from the lobes (right), with the East radio/X-ray hotspot and West radio hotspot labelled.

for standard Galactic gas/dust ratios. The true value is likely to lie somewhere between these extremes.

We therefore used our new data to estimate a column density directly. We extracted spectra for bright point sources around 3C 353 using local background regions. In Set 1 there were 5 point sources bright enough for spectroscopy. We fitted power-law models with free absorption to these sources and found a weighted mean $N_H = (1.64 \pm 0.07) \times 10^{21} \text{ cm}^{-2}$. As this is consistent with the range estimated above, we adopt the mean value in the analysis that follows.

The X-ray point sources are not shown in Fig. 3 and were excluded from all spectra extracted where the cluster was examined. The emission from the radio galaxy was also excluded.

3.2 The Nucleus

In the X-ray, the nuclear region was defined with a radius of 40 arcsec to include as many nuclear photons as possible while excluding the X-ray emission from the radio lobes. The background was estimated from a local background region positioned above the radio galaxy so as not to include any emission related to the radio galaxy. In the radio, the nuclear region was much smaller, adjusted in each data set to be a close fit to the nuclear emission. The peak intensity was determined using *jmfitt* for each frequency, the results of which are shown in Table 2.

We initially attempted to fit single power-law and thermal models to this spectrum; however, the fits were poor ($\chi^2 = 466.6$ for 259 d.o.f. and $\chi^2 = 2242.5$ for 259 d.o.f. respectively). We therefore fitted a model which has been shown (Hardcastle et al. 2006) to provide a good fit to the nuclear X-ray emission from

Table 2. Radio Core Fluxes

Band	Frequency (MHz)	Flux (Jy)	Luminosity ($\text{W Hz}^{-1} \text{ sr}^{-1}$)
P	327.3/329.6	0.097	1.5×10^{22}
-	620.5/633.3	0.089	1.4×10^{22}
L	1665/1678	0.116	1.8×10^{22}
C	4848/4898	0.140	2.2×10^{22}
X	8440/8452	0.149	2.3×10^{22}

narrow-line radio galaxies, consisting of a power-law component at Galactic absorption (see Section 3.1), a second power-law component with redshifted intrinsic absorption and a $kT = 1 \text{ keV}$ thermal component. The best fitting model had $\chi^2 = 268$ for 237 d.o.f. The core spectrum is shown in Fig. 4. The photon indices of the unabsorbed and absorbed power-law components were $\Gamma = 1.49 \pm 0.1$ and 1.33 ± 0.3 respectively, and the intrinsic column density was $6.1 \pm 0.6 \times 10^{22} \text{ cm}^{-2}$. The unabsorbed X-ray component has a 1 keV luminosity density of $1.86 \times 10^{16} \text{ W Hz}^{-1} \text{ sr}^{-1}$, whereas the absorbed X-ray component with the absorption removed and extrapolated to include energies from 2–10 keV has a luminosity of $2.82 \times 10^{42} \text{ erg s}^{-1}$. We discuss the interpretation of the nuclear emission in Section 4.1.

3.3 Lobe properties

By considering the X-ray emission from regions encompassing the east and west lobes but excluding the hotspots and the core, we extracted spectra from the combined X-ray data set using local back-

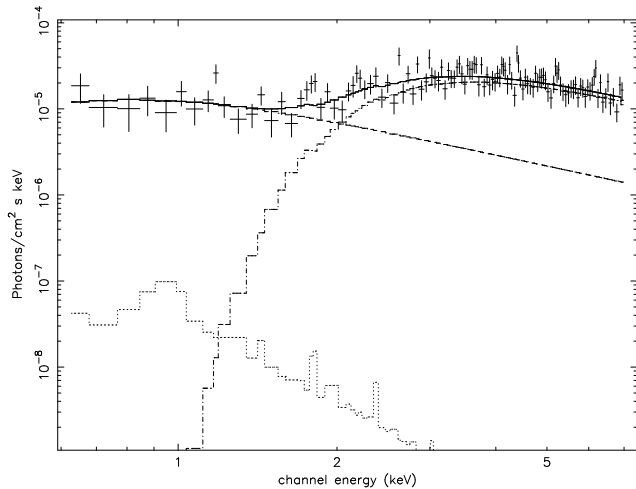


Figure 4. X-ray spectrum of the nucleus in the energy range 0.3–7.0 keV. The model plotted is the dual power-law + thermal model as described in Section 3.2. For clarity only the PN data are plotted.

ground regions which we fitted with both thermal emission models and power laws. Assuming a circularly symmetric model for the core, we determined that ~ 6 per cent of the counts in the East lobe spectra are from the core whereas the core counts account for a quarter of those in the West lobe spectra. Using the *XMM-Newton* calibration files, we determined the fraction of the core spectrum expected to be scattered into the West lobe region to be 4 per cent of the total core emission, and so we included a fixed component in the West lobe spectral fit consisting of the best-fitting core model with a normalisation fixed at 0.04 times that of the core. The details of the core spectrum are given in Section 3.2. Due to the low signal to noise of Set 2, the West lobe was undetected in this data set and so our spectra were extracted from Set 1 only.

The background emission from the cluster environment is the primary contributor to the uncertainty in the lobe flux densities. To best take account of this variation we used a truncated annular background region for the East lobe where the lobe appears to interact with the cluster. We investigated the effect of using local background regions above and below the galaxy; the best fitting power-law models gave consistent photon indices but led to an increase of a factor 2 in the flux density of the East lobe. These background regions only take account of the emission from one of the two sub-clusters leading us to believe that a truncated annular background region is a more accurate measure of the cluster’s contribution. For the West lobe, a local background region located to the south of the galaxy, at a similar distance from the brightest cluster emission took account of the emission from the southern sub-cluster sufficiently to allow a good fit to the spectra.

The power-law model gave better fits than the thermal model for both lobes with $\chi^2 = 39.6$ for 34 d.o.f for the East lobe and $\chi^2 = 23.1$ for 24 d.o.f for the west lobe. The photon indices were $\Gamma = 1.9 \pm 0.4$ and $\Gamma = 1.2 \pm 0.6$ respectively, corresponding to $\alpha = 0.9 \pm 0.4$ and $\alpha = 0.2 \pm 0.6$. Figure 5 shows the best-fitting power-law model for the East and West lobe X-ray data. The low frequency X-ray spectral index, measured between 327 MHz and 1.67 GHz, is ~ 0.7 for both lobes, so that the X-ray spectral indices of both lobes are consistent with a CMB inverse-Compton scattering model. We discuss the nature of the lobes in Section 4.2.

3.4 The nature of the hotspots

Both the East and West hotspots are clearly detected in all radio frequencies. The West hotspot is undetected in the X-ray; however, the East hotspot has an X-ray counterpart 6.5 ± 0.8 arcsec (4.0 ± 0.5 kpc) from the centre of the radio hotspot. This has too low signal to noise for spectral analysis to be performed, with only 60 counts between 0.3 and 7.0 keV. In recent *Chandra* observations (Kataoka et al., private communication), the same feature is detected but the offset was measured as 4.6 ± 0.5 arcsec. A jet knot was also detected in the vicinity of the East X-ray hotspot suggesting that the difference in our offset measurements could be due to contamination from this knot.

The inverse-Compton analysis performed on the lobes cannot be applied here as the electron populations responsible for any inverse-Compton X-ray and radio synchrotron emission reside in different regions. X-ray hotspots in radio galaxies of similar radio luminosity to 3C 353 are generally thought to be produced by synchrotron emission, and so this is likely to be the dominant emission process for this X-ray hotspot as well. The offsets measured between the X-ray and radio hotspots are consistent with what is seen in some other sources (Hardcastle et al. 2002, 2007; Erlund et al. 2007).

3.5 Cluster characterization

Unfortunately, the southernmost section of the southern sub-cluster extends beyond the field of view of the *XMM-Newton* cameras; however, a comparison to the *ASCA* image of Iwasawa et al. (2000) shows that the peak of the X-ray surface brightness is included in our data.

We extracted spectra from the northern and southern sub-clusters using a double subtraction method with annular local background regions. The northern and southern sub-cluster regions are shown in Fig. 7. Thermal models fitted using *mekal* in XSPEC give acceptable fits ($\chi^2 = 258$ for 175 d.o.f and $\chi^2 = 544$ for 490 d.o.f for the northern and southern sub-clusters respectively) with $kT = 3.3 \pm 0.3$ keV for the northern sub-cluster and $kT = 4.0 \pm 0.5$ keV for the southern sub-cluster both fitted with an absorption of $N_H = 1.6 \times 10^{21} \text{ cm}^{-2}$. The best-fitting models are shown in Fig. 6. Iwasawa et al. (2000) determined the temperature of the combined sub-clusters to be $kT = 4.3 \pm 0.2$ keV using a Galactic absorption of $N_H = 1.0 \times 10^{21} \text{ cm}^{-2}$ whereas when the upper limit ($1.6 \times 10^{21} \text{ cm}^{-2}$) was used, the temperature dropped to 3.94 ± 0.21 keV which is consistent with the mean temperature of the cluster. The difference in temperature of ~ 1 keV supports the idea that the two sub-clusters are originally separate components undergoing a merger. Taking a north-south slice through the cluster using rectangular regions of 208×104 arcsec from 17:20:50.074, -00:53:13.77 (Fig. 8), there is no evidence for a shock and no increase in surface brightness, indicating a non-violent interaction between these components.

A thermal model was fitted to annular regions in the northern and southern sub-clusters. The results are shown in Table 3. The residual local background was accounted for using regions in a relatively source free area of the field of view. Using an annular background region gave consistent temperatures for both sub-clusters. The northern sub-cluster shows a linear increase in temperature with radius with a best fit of $T(r) = 0.010r + 1.528$ keV while the southern sub-cluster is isothermal within the errors. 3C 353’s East lobe lies at a radius of 250 – 350 arcsec from the centre of the northern sub-cluster but it may also be affected by the south-

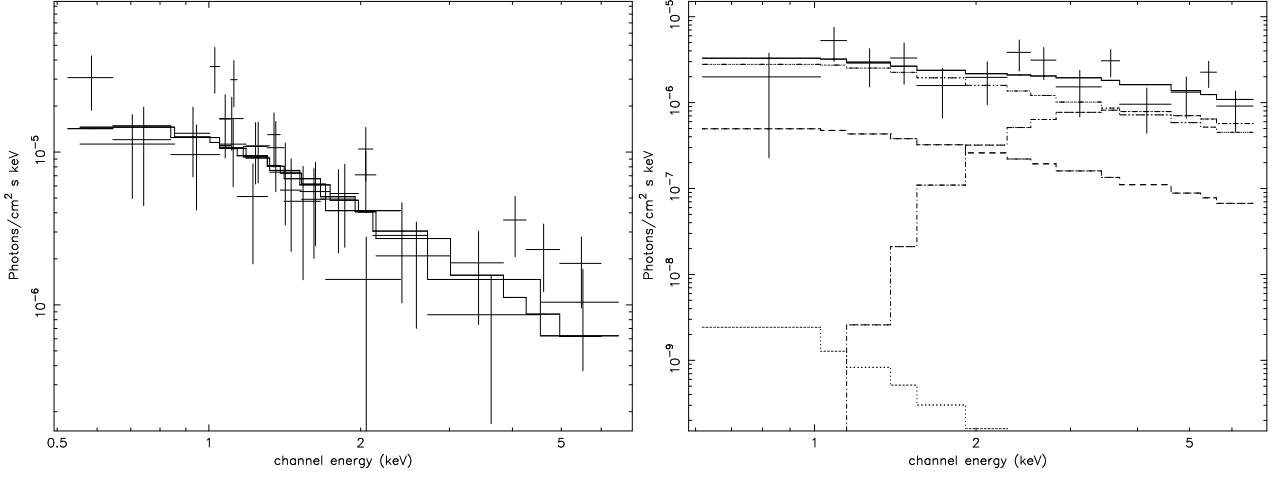


Figure 5. X-ray spectra for the East (left) and West (right) lobes in the energy range 0.3–7.0 keV. The East lobe shows the MOS 1, MOS 2 and PN cameras with the power-law model while the West lobe shows only the PN data for clarity with the dual power-law + thermal contribution from the core as well as the best-fitting power-law model from the lobe emission as described in Section 3.3.

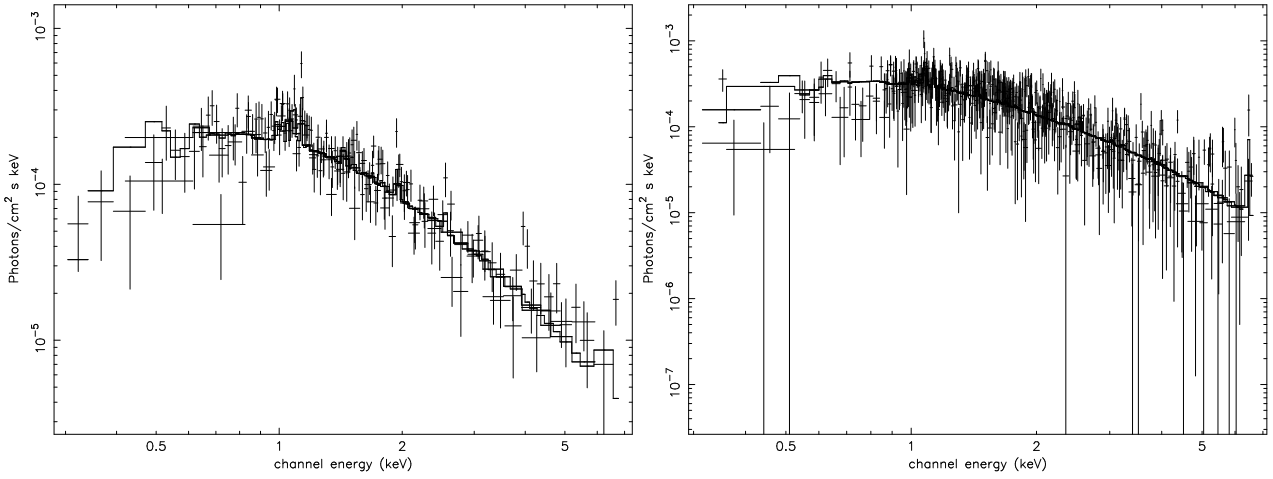


Figure 6. X-ray spectra for the northern (left) and southern (right) sub-clusters in the energy range 0.3–7.0 keV. The MOS1, MOS2 and PN data sets are shown in each case with the best-fitting thermal model as described in Section 3.5.

Table 3. Temperature profiles for the northern and southern sub-clusters

Radius (arcsec)	Northern kT (keV)	$\chi^2/\text{d.o.f.}$	Radius (arcsec)	Southern kT (keV)	$\chi^2/\text{d.o.f.}$
0 – 50	1.8 ± 0.3	29/19	0 – 75	5.2 ± 0.7	537/348
50 – 100	2.2 ± 0.3	121/65	75 – 150	4.2 ± 0.3	638/444
100 – 150	2.8 ± 0.4	130/102	150 – 200	4.7 ± 0.4	250/167
150 – 250	3.5 ± 0.3	129/108	200 – 250	4.9 ± 0.5	296/183
250 – 350	3.5 ± 0.5	286/172			

ern sub-cluster. The annular temperature at this radius ($kT = 3.5 \pm 0.5$ keV) is consistent with the global northern sub-cluster temperature ($kT = 3.3 \pm 0.3$ keV) as well as the temperature measured by the slice at this radius ($kT = 3.9 \pm 0.6$ keV). We therefore adopt a temperature of 3.5 ± 0.5 keV for the environment of 3C 353.

As 3C 353 interacts mainly with the northern sub-cluster and as the southern sub-cluster is not fully covered within the *XMM-Newton* field of view, surface brightness and pressure profiles were constructed for the northern sub-cluster only. To determine the cen-

tre of the northern sub-cluster we used a centroiding routine for each of the *XMM-Newton* cameras. Annular regions were used to extract a surface brightness profile, excluding the chip gaps, X-ray point sources, emission from 3C 353 and from the southern sub-cluster and the position of the missing chip in the MOS 1 camera. An annular region was used to account for the residual local background emission. The surface brightness profiles for each camera were fitted with a model consisting of a β model convolved with the *XMM-Newton* PSF based on the on-axis parametrisation described in the *XMM-Newton* CCF files XRT1_XPSF_0006.CCF, XRT2_XPSF_0007.CCF and XRT3_XPSF_0007.CCF before being fitted with a β model (Fig. 9).

We examined the annuli in quadrants to highlight any density variation in a north-south or east-west direction. The northern quadrants and the south-east quadrant were consistent. We excluded the south-west quadrant from the final profile to ensure that X-ray emission from the radio galaxy, and any local disturbances in the cluster gas, were removed. The resulting surface brightness profiles were consistent for all cameras. The joint best-fitting model, for all cameras, had a radius of 194 arcsec and $\beta = 0.35$. Considering a 1σ confidence interval for 2 interesting parameters, β was

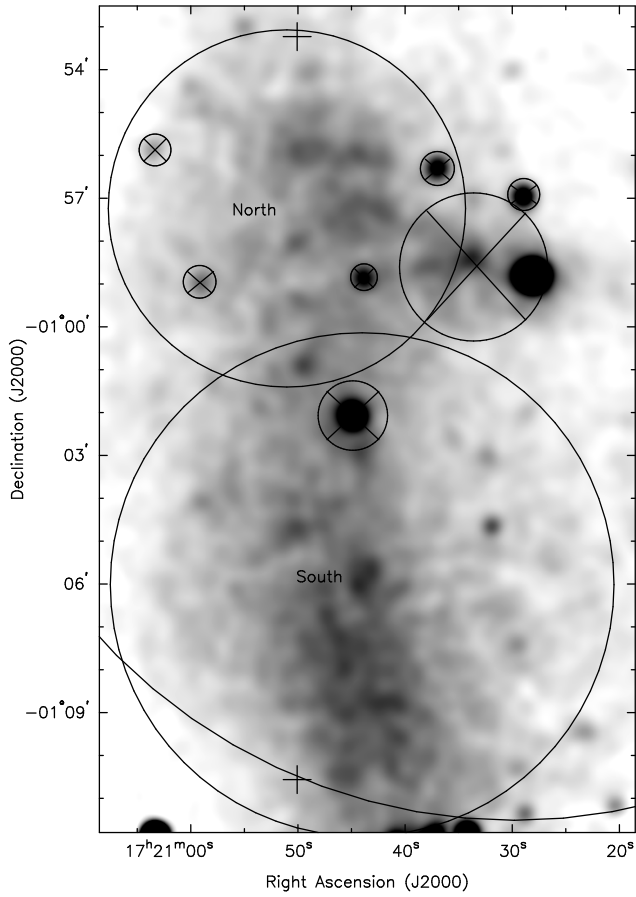


Figure 7. Northern and southern sub-cluster regions from which spectra were extracted to determine the sub-cluster global temperatures. The crossed regions are those which were excluded from the analysis and include the X-ray point sources and 3C 353. The crosses indicate the limits of the slice used. The inner edge of a large annular region masking the edge of the camera can be seen at the bottom of the image.

unconstrained (though we consider values below 0.35 and above 0.9 unrealistic), whereas the core radius of the northern sub-cluster was limited to between 184 and 412 arcsec. We discuss the results of this section in Section 4.3.

4 DISCUSSION

4.1 The nature of the core

The double-peaked nuclear X-ray spectrum, consisting of a heavily absorbed component together with one with only Galactic absorption, is typical of what is observed in narrow-line radio galaxies (NLRG) (e.g. Sambruna, Eracleous & Mushotzky 1999; Grandi, Malaguti & Fiocchi 2006; Belsole, Worrall & Hardcastle 2006; Hardcastle, Evans & Croston 2006). However, when we plot the unabsorbed luminosity of the heavily absorbed nuclear component in 3C 353 against its 178-MHz total radio luminosity, as done by Hardcastle et al. (2006) (their figure 3) we find that 3C 353 lies almost 1 order of magnitude below the correlation they determined for NLRGs: that is, 3C 353 is overluminous in the radio for its X-ray luminosity or underluminous in the X-ray for its radio luminosity, and lies closer to the region of the plot occupied by low-excitation radio galaxies (LERGs). By contrast, the unab-

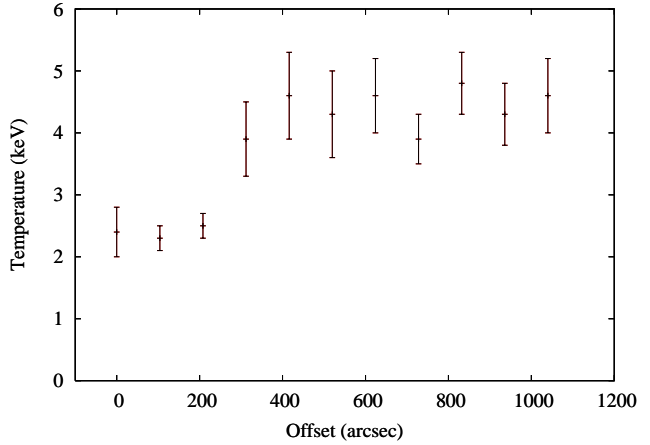


Figure 8. Temperature variation of north-south slice through cluster with rectangular regions of 208×104 arcsec from a zero of offset at 17:20:50.074, -00:53:13.77.

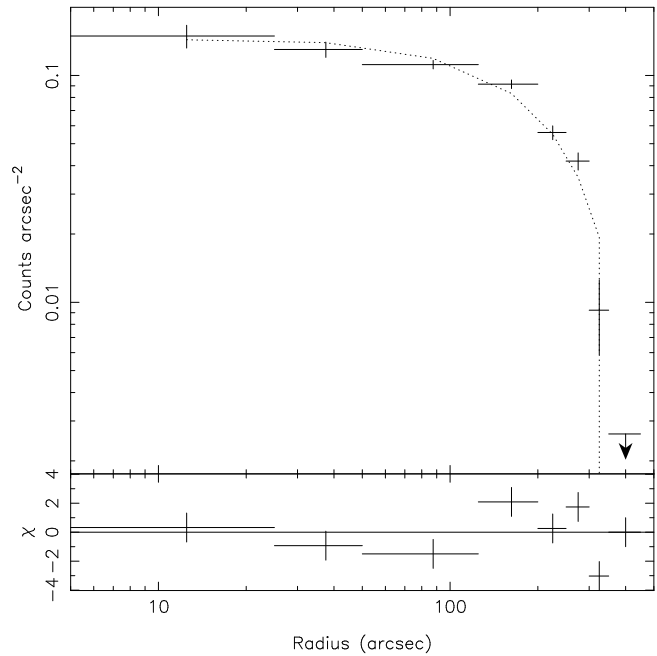


Figure 9. Surface brightness profile for the northern sub-cluster showing the PN data set with the best-fitting β model which has $\beta = 0.35$ and core radius 194 arcsec.

sorbed component is consistent with the correlation found by Hardcastle et al. between unabsorbed X-ray luminosity and nuclear 5-GHz radio emission (their figure 3).

The optical emission-line classification of 3C 353 is uncertain. Laing et al. (1994) use the ratio of the flux in the [O III] line to that in the $H\alpha$ to distinguish between the NLRGs and LERGs. The best published optical spectrum of 3C 353 is that of Simpson et al. (1996), and their quoted line fluxes clearly place 3C 353 below the [O III]/ $H\alpha$ cutoff of 0.2 proposed by Laing et al: thus by this definition 3C 353 would be a LERG. However, if the line fluxes are corrected for reddening using values determined from the Schlegel, Finkbeiner & Davis (1998) dust maps (see Section 3.1), then the emission-line ratio rises to 0.17 ± 0.02 , where the errors are derived from the normal 10 per cent errors of Simp-

son et al. and are almost certainly too low: within the errors we cannot say whether 3C 353 should be classed as a LERG or NLRG. The nature of 3C 353's nucleus both in the optical and in the X-ray remains ambiguous.

4.2 Lobe emission and properties

Using the method of Croston et al. (2005), the X-ray observations were compared to the predictions of an inverse-Compton model, based on synchrotron modelling of the radio data sets using SYNCH (Hardcastle et al. 1998). The broad-band spectra for the lobes are shown in Fig. 10. The measured 1-keV flux densities of the East and West lobes are 11.6 ± 1.6 and 2.7 ± 1.0 nJy. The equipartition magnetic field strengths for the East and West lobes are 0.89 nT and 0.84 nT respectively, while if we assume that all the X-ray emission is inverse-Compton in origin then the measured flux densities correspond to magnetic field strengths of 0.44 ± 0.06 nT and 0.68 ± 0.2 nT. Therefore, while the weakly detected West lobe has a measured magnetic field strength within errors of the predicted equipartition value, the East lobe's measured magnetic field strength exceeds the predicted equipartition value by a factor ~ 2 so that $B_{\text{obs}}/B_{\text{eq}} \simeq 0.4$. The West lobe's measured magnetic field strength is also consistent with a substantial departure from equipartition. This implies that the lobes of 3C 353 are electron dominated, which is not unusual considering the range of field strengths in the sample of Croston et al. (2005). This factor would be reduced for 3C 353 if the lobes were not in the plane of the sky.

The measured magnetic field strengths in the lobe correspond to internal pressures of $3.4 \pm 0.6 \times 10^{-13}$ Pa and $1.9 \pm 0.2 \times 10^{-13}$ Pa for the East and West lobes respectively. (If the alternative local background regions discussed in Section 3.3 were used, the magnetic field strengths would be reduced by ~ 0.1 nT and the internal pressure of the East lobe would double, but this does not affect our conclusions.)

Using the radio data sets, we constructed a spectral index map between the 1.67-GHz and 327-MHz images, Fig 11. It revealed a variation of $\Delta\alpha \sim 0.2$ across both lobes. Within the radio luminous region of the East lobe, excluding the hotspots, the spectral index is roughly constant, $\alpha = 0.66 \pm 0.01$ despite the filamentary structure seen in Fig. 1, whereas in the West lobe, $\alpha = 0.63 \pm 0.01$ excluding the hotspot. We note that the radio lobes do not appear to be entirely separate, and thus consider the region in between the radio luminous lobes, north and south of the core to be an inter-lobe region, which cannot be unambiguously associated with either lobe. This inter-lobe region has a relatively steep spectrum of $\alpha = 0.75 \pm 0.01$ whereas the hotspot in both lobes exhibits a flatter spectrum of $\alpha = 0.60 \pm 0.01$. Fig. 11 shows the spectral index map between 1.67 GHz and 327 MHz with contours from the 327-MHz map.

The X-ray/radio ratio was determined for the hotspot, lobe and inter-lobe regions, using the high signal to noise of the X-ray data set. The 327 MHz radio map of resolution 7.0×7.0 arcsec was used with the convolved, exposure corrected X-ray map of energies 0.3 to 7.0 keV. The X-ray/radio ratio was found to be a factor of 4 greater in the steep inter-lobe region than in the flat, hotspot regions. If the magnetic field strength and the number densities of both the inverse-Compton and synchrotron emitting electron are constant across the lobe, the X-ray/radio ratio would also be constant, but this is not what we see in 3C 353. Similar results have been seen in other radio galaxies, notably 3C 452 (Isobe et al. 2002) and Pictor A (Hardcastle & Croston 2005). Hardcastle &

Croston consider the following three models to explain the varying X-ray/radio ratio:

- (i) Some other emission process could boost the X-ray emission in the inner regions;
- (ii) The central regions contain more low-energy electrons relative to the outer regions;
- (iii) The magnetic field strength varies as a function of position.

A contribution from the core was included in the X-ray spectral analysis which also takes account of the contribution of the unabsorbed X-ray emission associated with the jet and the absorbed X-ray emission from the accretion disk. Emission from the core cannot therefore boost the X-ray emission in the inner regions. Our spectral fits show no evidence for a contamination of the lobe spectra by galaxy-scale thermal emission. Neither could a boost be due to the galaxy's proximity to the cluster as local background regions were used to account for any thermal emission from the sub-clusters. For inverse-Compton scattering of nuclear photons to be the dominant process, the core bolometric luminosity needs to be at least 10^{38} W. This is not unrealistic, however modelling the lobe surface brightness for this scenario using the results of Brunetti (2000) as described by Hardcastle et al. (2002) and with 3C 353 in the plane of the sky, reveals a gradient across the lobe which is not observed in either the X-ray image nor the X-ray/radio ratio. Using the spectral energy distributions of Haas et al. (2004), we deduced a typical IR spectrum for 3C 353 by scaling a dual power-law fit to the spectral energy distribution of 3C 33. 3C 33 was chosen as it has a similar luminosity and is classified as a NLRG/FR II. The IR spectrum was normalised by the ratio of low-frequency radio luminosities of the two sources. The predicted flux density for the nuclear inverse-Compton emission is 6.5×10^{-12} Jy at 1 keV, which is a factor of ~ 700 fainter than the predicted CMB inverse-Compton emission and the observed flux density (4.4 and 11.6 nJy respectively). Thus we can rule out model (i).

If we consider the magnetic field to be constant at the measured lobe averaged magnetic field strength of 0.39 nT and apply an inverse-Compton model to the lobes, we find the emission at 327 MHz traces electrons with $\gamma \simeq 4000$ whilst the measured inverse-Compton emission traces electrons at $\gamma \simeq 1000$. As the critical frequency for synchrotron emission goes as γ^2 , we find that a variation in the X-ray/radio ratio of a factor of 4 requires a variation in the spectral index between 10 MHz and 327 MHz of ~ 0.5 . Even if the equipartition magnetic field strength of 0.89 nT is assumed so that the 327 MHz emission traces electrons of $\gamma \simeq 3000$, the observed spectral index variation requires a factor ~ 1.2 variation in the X-ray/radio ratio which is still much lower than observed. This is also the case with Pictor A (Hardcastle & Croston 2005); a variation in the low-energy electron densities alone (model ii) cannot explain the variation of X-ray/radio ratio across the lobe.

Alternatively, if we assume constant electron densities for both the synchrotron and inverse-Compton emission electrons and also that the magnetic field strength does not vary along the line of sight, we find that the observed variation in the X-ray/radio ratio then requires a variation in the magnetic field of at most a factor of 2.5. For a given frequency, this means the spectral index observed at low frequencies, between 1.67 GHz and 327 MHz, for regions of high X-ray/radio ratio should correspond to the spectral index between 3.5 GHz and 825 MHz for low X-ray/radio ratio regions. We consider the spectral indices between 4.8 GHz and 1.67 GHz to limit the spectral indices of the low X-ray/radio ratio regions and find that they exceed the upper limit predicted by the observed X-ray/radio ratio. From this comparison, we cannot rule out the pos-

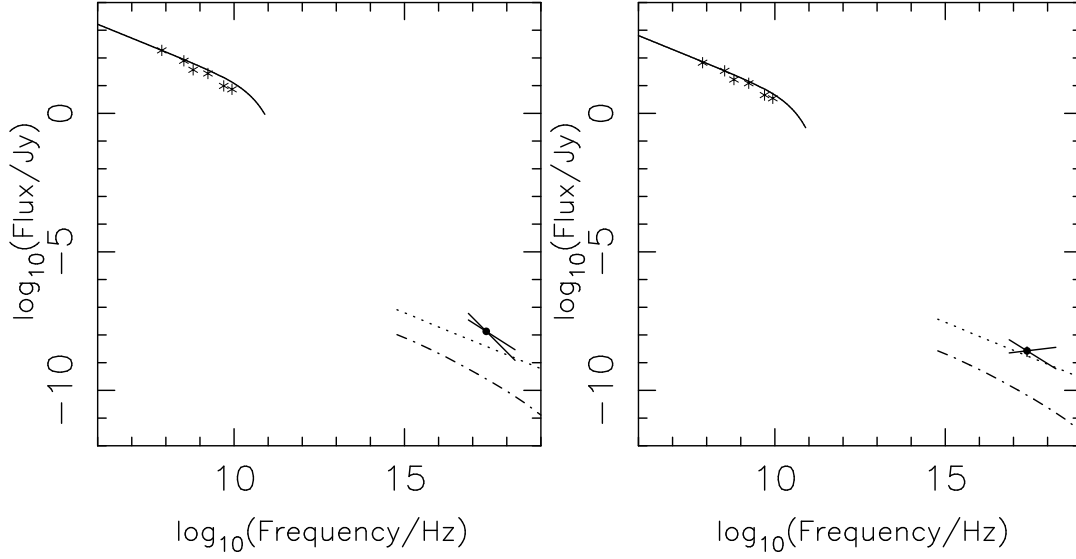


Figure 10. Broad-band spectrum for the East (left) and West (right) lobes of 3C 353. A synchrotron emission model (solid line) is fitted to the radio data (asterisks). The measured X-ray flux is represented by the dot with the bowtie indicating the error. The dotted line shows the inverse-Compton X-ray flux prediction and the dash-dotted line shows the predicted synchrotron self-Compton emission, both with the equipartition magnetic field strength.

sibility that a varying magnetic field alone could be responsible for the observed variations in the X-ray/radio ratio and the spectral indices. We therefore considered a colour-colour diagram using the method of Katz-Stone, Rudnick & Anderson (1993). In their study of Cygnus A, they argue that a single curve on a colour-colour diagram is consistent with a homogeneous distribution of relativistic electrons together with varying the magnetic field strength across the source. The colour-colour diagram for 3C 353, shown in Fig. 12, has a similar single curve and so is consistent with this picture. In Pictor A, Hardcastle & Croston (2005) argued that the detailed positional variations of radio spectra and radio/X-ray ratio were not consistent with such a model, but our data are not good enough to rule it out here.

We conclude that a varying electron spectrum alone cannot account for the observed variation in X-ray/radio ratio in the lobes of 3C 353 but that a magnetic field strength that varies by a factor of ~ 2.5 throughout the lobes can explain it. Similar conclusions were reached by Hardcastle & Croston (2005) in their study of Pictor A.

4.3 The cluster-lobe interaction

The surface brightness profile was converted to a pressure profile using the method of Birkinshaw & Worrall (1993), so that the radio lobe pressures determined with SYNCH could be directly compared to the external pressure from the cluster at the position of the radio galaxy. The centre of the East lobe lies ~ 280 arcsec from the centre of the northern sub-cluster. At this radial distance where the temperature of the environment is taken as 3.5 ± 0.5 keV, the external pressure is much greater than the internal pressure of the lobes (See Fig. 13). As FR II radio galaxies are expected to be in pressure balance or over pressured, either 3C 353 is not in the plane of the cluster or there is an additional contribution to the pressure from non-radiating particles such as hot thermal or relativistic protons in the lobes. Previous studies of FR II radio galaxies in groups and clusters have shown that pressure balance can usually be achieved without additional protons (e.g. Croston et al. 2005; Hardcastle et al. 2002; Belsole et al. 2004). We therefore assume

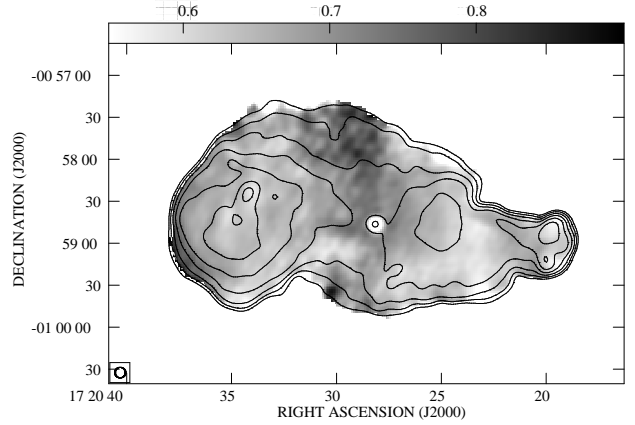


Figure 11. Spectral index map between 1.67 GHz and 327 MHz with radio contours at 327 MHz for levels of $0.01 \times (1, 2, 4, \dots)$ mJy/beam. The beam size is shown by the circle in the bottom left corner and the colour bar at the top shows the mapping of the grey levels to spectral index.

that 3C 353 is not in the plane of the cluster and using the East lobe, determine that 3C 353 requires a shift in radial position corresponding to ~ 600 arcsecs to be in pressure balance with the northern sub-cluster (here we use the best estimate of the lobe pressure from Section 4.2). This places 3C 353 ~ 370 kpc either in front or behind the centre of the cluster. At this position, the West lobe's internal pressure is also consistent with the intracluster pressure. The position of 3C 353 with respect to the pressure profile is shown in Fig. 13. At this distance from the cluster, the external pressures seen by the lobes are different by a factor of ~ 1.8 , which may help to explain the difference in appearance of the lobes, the East having a spherical appearance whilst the West lobe is elongated with hotspots at the outer edge.

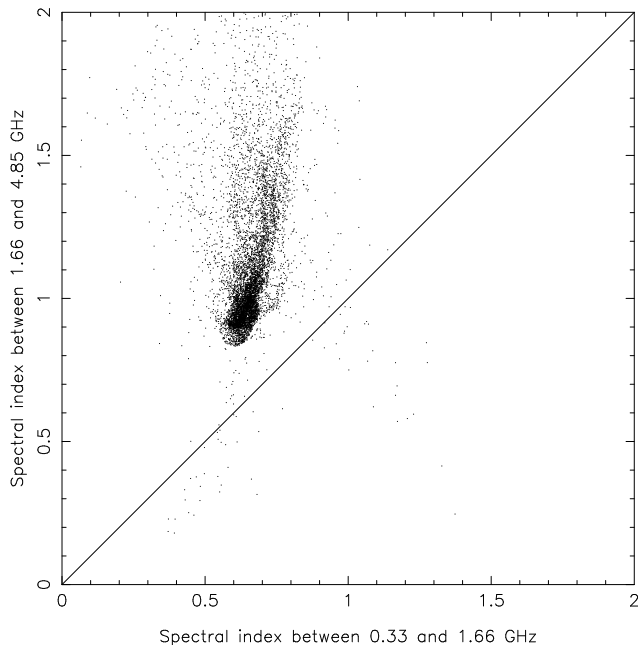


Figure 12. Colour-colour diagram for 3C 353 made at 7 arcsec resolution.

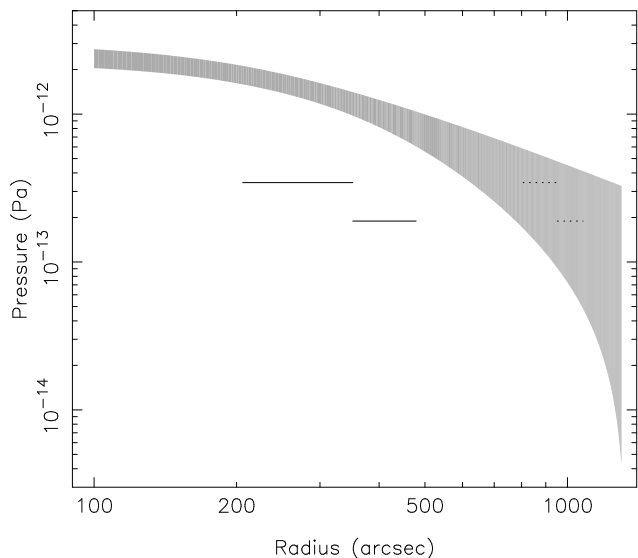


Figure 13. Pressure profile for the northern sub-cluster shown by the greyed in region, with the measured pressure of the lobes of 3C 353 at the projected distance (solid line) and at the position with the radial shift applied to where the East lobe is in pressure balance with the sub-cluster (dashed line). The measured inverse-Compton emission was used to determine the pressure within each lobe. The temperature of the cluster at the radial distance of 3C 353 was used.

4.4 Additional features of note

In addition to the usual radio-lobe structure, the East lobe of 3C 353 contains a dark circular region of unknown origin at 17:20:36.088, -00:58:44.15 (Fig. 1). Detectable in all radio frequencies except 74 MHz (presumably due to its low resolution), the measured fluxes in this region are a factor of 100 above the rms background but are a factor of 2 fainter than the surrounding lobe emission. The X-ray image shows no sign of any feature in this region and neither does the Digital Sky Survey (DSS). As the level of the deficit is inde-

pendent of frequency we can rule out an foreground absorber and the required geometry is unrealistic for an obstruction in the lobe. Without further information we are unable to identify this feature.

Iwasawa et al. (2000) included optical observations of the cluster region centred on 3C 353 taken with the University of Hawaii 2.2 m telescope in their analysis of Zw 1718.1-0108. They identified three additional massive galaxies, none of which reside in the northern sub-cluster. Deeper optical observations would help to establish whether there are any galaxies associated with the northern sub-cluster and whether 3C 353 is the dominant member of this sub-cluster despite its position at the edge.

5 SUMMARY AND CONCLUSIONS

Our results can be summarized as follows:

- By fitting an inverse-Compton model to the lobes, we found the East lobe to be electron dominated and the West lobe to be consistent (within the large errors) with equipartition.
- We determined that a variation in the electron spectrum cannot account for the varying X-ray and radio emission alone, but that a change in the magnetic field strength across the lobes is required.
- We have obtained a good X-ray spectrum of the nucleus of 3C 353. Both the X-ray and optical properties of this source are ambiguous but it appears to lie in a region of parameter space in between those normally occupied by narrow-line and low-excitation radio galaxies.
- We have detected an X-ray counterpart for the East hotspot offset by 4.0 ± 0.5 kpc.
- The northern and southern sub-clusters were found to be isothermal with a temperature difference of ~ 1 keV supporting a model in which they are two originally separate components undergoing a merger with no evidence for a violent interaction.

ACKNOWLEDGEMENTS

JLG thanks the STFC for a research studentship. MJH acknowledges generous financial support from the Royal Society. We also thank Jun Kataoka and the anonymous referee for helpful advice and comments. The National Radio Astronomy Observatory is a facility of the National Science Foundation operated under cooperative agreement by Associated Universities, Inc. We thank the staff of the GMRT for their help with the observations with that telescope: GMRT is run by the National Centre for Radio Astrophysics of the Tata Institute of Fundamental Research, India. This work is partly based on observations obtained with *XMM-Newton*, an ESA science mission with instruments and contributions directly funded by ESA Member States and NASA. Basic research in radio astronomy at the Naval Research Laboratory is supported by 6.1 basic research.

REFERENCES

- Arnaud, M. et al., 2002, *A&A* 390, 27
 Belsole, E., Worrall, D.M., Hardcastle, M.J., Birkinshaw, M. & Lawrence, C.R., 2004, *MNRAS* 352, 924
 Besole, E., Worrall, D.M. & Hardcastle, M.J., 2006, *MNRAS* 366, 339
 Birkinshaw, M. & Worrall, D.M., 1993, *ApJ* 412, 568
 Brunetti, G., Setti, G. & Comastri, A., 1997, *A&A* 325, 898

- Brunetti, G., 2000, *Astropart. Phys.*, 13, 107
- Croston, J.H., Hardcastle, M.J., Birkinshaw, M. & Worrall, D.M., 2003, *MNRAS* 346, 1041
- Croston, J.H., Hardcastle, M.J., Harris, D.E., Belsole, E., Birkinshaw, M. & Worrall, D.M., 2005, *ApJ* 626, 733
- Dickey, J.M. & Lockman, F.J., 1990, *ARAAS* 28, 215
- Erlund, M.C., Fabian, A.C., Blundell, K.M., Moss, C. & Ballantyne, D.R., 2007, *MNRAS* 379, 498
- Fanaroff B.L. & Riley, J.M., 1974, *MNRAS* 167, 31P
- Feigelson, E.D., Laurent-Muehleisen, S.A., Kollgaard, R.I. & Formanont, E.B., *ApJ* 449, L149
- Grandi, P., Malaguti, G. & Fionchi, M., 2006, *ApJ* 642, 113
- Haas, M. et al., 2004, *A&A* 424, 531
- Hardcastle, M.J., Birkinshaw, M. & Worrall, D.M., 1998a, *MNRAS* 294, 615
- Hardcastle, M.J., Birkinshaw, M., Cameron, R.A., Harris, D.E., Looney, L.W. & Worrall, D.M., 2002, *ApJ* 581, 948
- Hardcastle, M.J. & Croston, J.H., 2005, *MNRAS* 363, 649
- Hardcastle, M.J., Evans, D.A. & Croston, J.H., 2006, *MNRAS* 370, 1893
- Hardcastle, M.J., Kraft, R.P., Worrall, D.M., Croston, J.H., Evans, D.A., Birkinshaw, M. & Murray, S.S., 2007, *ApJ* 662, 166
- Isobe, N., Tashiro, M., Makishima, K., Iyomoto, N., Suzuki, M., Murakami, M.M., Mori, M. & Abe, K., 2002, *ApJ* 580, L111
- Iwasawa, K., Etori, S., Fabian, A.C., Edge, A.C. & Ebeling, H., 2000, *MNRAS* 313, 515
- Kassim, N.E. et al., 2007, preprint (astro-ph/0704.3088)
- Katz-Stone, D.M., Rudnick, L. & Anderson, M.C., 1993, *ApJ* 407, 549
- Kataoka, J. & Stawarz, L., 2005, *ApJ* 622, 797
- Laing, R.A., Jenkins, C.R., Wall, J.V. & Unger, S.W., 1994, *ASPC* 54, 201
- Lazio, T.J.W., Kassim, N.E., and Perley, R.A. 2005, *Low-Frequency Data Reduction at the VLA: A Tutorial for New Users*
- Mackay, C.D., 1973, *MNRAS* 162, 1
- Read, A.M. & Ponman, T.J., 2003, *A&A* 409, 395
- Sambruna, R.M., Eracleous, M. & Mushotzky, R.F., 1999, *ApJ* 526, 60
- Schlegel, D.J., Finkbeiner, D.P. & Davis, M., 1998, *ApJ* 500, 525
- Simpson, C., Ward, M., Clements, D.L. & Rawlings, S., 1996, *MNRAS* 281, 509
- Swain, M.R. 1996 Ph.D. thesis, Univ. Rochester
- Swain, M.R., Bridle, A.H. & Baum, S.A., 1998, *ApJ* 507, L29
- Tashiro et al. 1998, *ApJ* 499, 713
- Tashiro, M., Makishima, K., Iyomoto, N., Isobe, N. & Kaneda, H., 2002, *ApJ* 526, L19